AIAA SciTech Forum
January 3-7, 2022, San Diego, CA & Virtual
AIAA SCITECH 2022 Forum

10.2514/6.2022-0056

Aero-Optical Distortions of Turbulent Boundary Layers: Hypersonic DNS

Nathan E. Miller *, Kyle P. Lynch †
Sandia National Laboratories, Albuquerque, NM, 87185

Stanislov Gordeyev ‡
Notre Dame University, Notre Dame, IN 46556

Daniel R. Guildenbecher §
Sandia National Laboratories, Albuquerque, NM, 87185

Lian Duan ¶
The Ohio State University, Columbus, OH 43210

Ross M. Wagnild ‖
*Sandia National Laboratories**, *Albuquerque, NM, 87185*

Four Direct Numerical Simulation (DNS) datasets covering effective freestream Mach numbers of 8 through 14 are used to investigate the behavior of turbulence-induced aero-optical distortions in hypersonic boundary layers. The datasets include two from simulations of flat plate boundary layers (Mach 8 and 14) and two from simulations of flow over a sharp cone (Mach 8 and 14). Instantaneous three-dimensional fields of density from each DNS are converted to refraction index and integrated to produce distributions of the Optical Path Differences (OPD) caused by turbulence. These values are then compared to experimental data from the literature and to an existing model for the root-mean-square of the OPD. Although the model was originally developed for flows with Mach ≤ 5, it provides a basis to which we compare the hypersonic data.

Nomenclature

Ap	Aperture size
B	Modeling constant (= 0.2)
C_f	Coefficient of friction (= $2\tau_w/(\rho_e U_e^2)$)
c_p	Specific heat at constant pressure
F	Notre Dame model function
h_0	Total enthalpy (= $c_p T + \overline{U}^2/2$)
K_{GD}	Gladstone-Dale coefficient
Ma	Mach number
n	Index of refraction
OPD	Optical Path Difference
OPL	Optical Path Length
r	Recovery factor

*Senior Member of the Technical Staff, Aerosciences Department, AIAA Member, nmille1@sandia.gov
†Senior Member of the Technical Staff, Aerosciences Department, AIAA Member, klynch@sandia.gov
‡Associate Professor, Aerospace and Mechanical Engineering, AIAA Associate Fellow, sgordeye@nd.edu
§Principal Member of the Technical Staff, Diagnostic Sci. & Engineering, AIAA Senior Member, drguild@sandia.gov
¶Associate Professor, Mechanical and Aerospace Engineering, AIAA Associate Fellow, duan.322@osu.edu
‖Principal Member of the Technical Staff, Aerosciences Department, AIAA Associate Fellow, rmwagni@sandia.gov

**Sandia National Laboratories is a multimission laboratory managed and operated by National Technology & Engineering Solutions of Sandia, LLC, a wholly owned subsidiary of Honeywell International Inc., for the U.S. Department of Energy's National Nuclear Security Administration under contract DE-NA0003525. This paper describes objective technical results and analysis. Any subjective views or opinions that might be expressed in the paper do not necessarily represent the views of the U.S. Department of Energy or the United States Government.

R	Gas constant
Re_{Ap}	Reynolds number based on the aperture size (= $U_\infty Ap/\nu_\infty$)
Re_δ	Reynolds number based on the boundary layer thickness (= $U_\infty \delta/\nu_\infty$)
Re_θ	Momentum thickness Reynolds number (= $U_\infty \theta/\nu_\infty$)
T	Temperature
$\{x, y, z\}$	Streamwise, wall-normal, and spanwise coordinates, respectively
u'	Turbulent fluctuations of the streamwise velocity
$\overline{U}$	Reynolds-averaged streamwise velocity
γ	Specific heat ratio
δ	Boundary layer thickness
θ	Momentum thickness
μ	Dynamic viscosity
ν	Kinematic viscosity (= μ/ρ)
ρ	Density
τ_w	Wall shear stress $\left(= \mu_w \frac{\partial \overline{U}}{\partial y}\big\vert_w\right)$

Sub/superscript

cdf	Cumulative density function
e	Boundary layer edge value
i	Inflow condition
r	Recovery value
rms	Root-mean-square
w	Wall value
∞	Values outside the boundary layer (inside the shock layer in the cone cases)

I. Introduction

When collimated light passes through variations in the index of refraction (n) it experiences distortions to its planar wavefront as the phase of each individual ray within the beam is modulated. In high speed flows, variations in n can be caused by turbulent density fluctuations leading to aero-optical aberrations that can cause problems for communications, directed energy, and navigation [1].

When integrated along a beam path, these turbulence-induced optical aberrations alter the effective total pathlength along which the beam travels. The Optical Path Length (OPL) is the effective length that individual rays of light travel over while passing through the turbulent density fields and is defined as,

$$OPL(x, z, t) = \int_0^L n(x, y, z, t) ds, \tag{1}$$

where the integration is along the ray path (s) from the wall to some distance, L. For attached turbulent boundary layer (TBL) flows, this path is typically from the wall into the freestream or vice versa, and may be in the wall-normal direction or along some other angled direction, depending on the application. Given that n = 1.0 for light in a vacuum and is greater than one in any typical fluid medium, the OPL will always be longer than the actual physical distance from the wall to the freestream. For higher speed flows, where the density typically decreases significantly near the wall, the OPL is shorter than in an otherwise identical, but slower (and therefore denser), TBL flow. The local index of refraction within the TBL is linearly related to the local density via the Gladstone-Dale relation as,

$$n = 1 + K_{GD}\rho, \tag{2}$$

where K_{GD} is the Gladstone-Dale coefficient. K_{GD} varies somewhat at high temperature, varies across gas species, and varies with wavelength but a value of 2.35e-4 m^3/kg was used here and was chosen as it should be sufficiently accurate for the temperatures and gases used (air and nitrogen)[2, 3].

By then removing the mean behavior of the OPL within the aperture (or across the DNS domain as defined here) from the OPL field, the remainder is the two-dimensional field of wave-front aberrations imposed onto the otherwise

planar wave front by the fluctuating densities. This is called the Optical Path Difference (OPD) and, for data where a mean tilt is present, is defined as,

$$OPD = OPL - (m_x x + m_z z + b), \tag{3}$$

where m_x, m_z, and b are determined by minimizing,

$$R = \int_x \int_z (OPL - (m_x x + m_z z + b))^2 dx dz, \tag{4}$$

and x and z are the streamwise and spanwise coordinates of the aperture, respectively, following Wang and Wang [4]. The root-mean-square of the resulting distribution of OPDs (OPD_{rms}) is often used as the target variable for describing the aero-optical properties of a TBL [5].

While theoretical models for OPD_{rms} can be traced back to at least the 1960s [6] the model proposed by Gordeyev et al. [7] and used in a number of follow-up papers (e.g., [8]) is perhaps the most developed. It, like others (e.g., [9]), is based on the "linking equation" that can be traced back to the work of Sutton [6]. The linking equation has been validated experimentally [10] and takes the form of,

$$OPD_{rms}^2 = 2K_{GB}^2 \int_0^L \rho_{rms}^2(y) \Lambda_\rho(y) dy, \tag{5}$$

where Λ_ρ is the density correlation length. Gordeyev et al. [7] used a set of substitutions to allow for ρ_{rms} and Λ_ρ to be approximated from known flow quantities. If a flow is adiabatic and fluctuations of the pressure can be assumed to be negligible within the boundary layer, the model becomes,

$$OPD_{rms} = K_{GD} \rho_\infty M a_\infty^2 C_f^{0.5} \delta F(M a_\infty), \tag{6}$$

where C_f is the coefficient of friction on the wall, δ is the boundary layer (BL) thickness, $F(Ma_\infty) = B \cdot C(Ma_\infty)/C(0)$, B is a constant (determined to be 0.2), and $C(Ma_\infty)$ is a function based on the integration of TBL profiles and varies with the Mach number just outside the TBL (Ma_∞). This model will be referred to as the Notre Dame (ND) model for the remainder of this work. When a flow is non-adiabatic, the heating or cooling of the wall can have the effect of increasing or decreasing, respectively, density fluctuations in the boundary layer and similarly impacting the OPD_{rms} [11]. For such a situation, an alternate version of Eqn. 6 can be derived that does not assume away the difference in the recovery and wall temperatures ($\Delta T = T_w - T_r$) and which maintains the effects imposed by pressure fluctuations (which become more important for cooled walls). This results in,

$$OPD_{rms} = A_0 K_{GD} \rho_\infty C_f^{0.5} \delta \left[M_\infty^4 + C_1 \frac{\Delta T}{T_\infty} M_\infty^2 + C_2 \left(\frac{\Delta T}{T_\infty} \right)^2 \right]^{1/2}, \tag{7}$$

where A_0, C_1, and C_2 are all based on profile integrations (like $F(Ma_\infty)$) and include the effects of pressure fluctuations. For self-similar flows, A_0, C_1, and C_2 are essentially constant but may vary somewhat in real flows as functions of Ma_∞ and ΔT [11]. Investigation of the behavior of the TBL profiles, the assumptions made in the derivation of these models, and the functional dependencies of OPD_{rms} in hypersonic flows is the focus of this and other related works (e.g., [12–14]).

Most previous studies of OPD_{rms}, both computational and experimental, have not exceeded Mach numbers of ≈ 6, with one notable exception being the experiment of Wyckham and Smits [9] at Mach 7.8. In previous papers Miller et al. [12] and Lynch et al. [15], computational and experimental results up to a Mach 8 were reported. Miller et al. [12] used four Direct Numerical Simulation (DNS) datasets at different Mach numbers both to corroborate the behavior of the ND model at subsonic and supersonic Mach numbers but also to extend the studied envelope of OPD_{rms} to both TBL flows over a sharp cone and to the higher Mach number of 8. The development of the ND model was based on subsonic and supersonic TBL flows and while it has demonstrated good results up to Mach 4.5 [16] an expected divergence between the model and studied data is observed at Mach > 6 [15, 17].

Herein, four DNS datasets are used to investigate OPD properties of TBLs at hypersonic Mach numbers for two flow geometries. Additionally, these datasets come from simulations run with iso-thermal (cooled) walls and thus provide another degree of difference from the assumptions used in the model development. Two of the included datasets are the two hypersonic sets used in Miller et al. [12], specifically, a Mach 8 flat plate TBL and a 7° sharp cone simulated with the Mach 8 flow conditions seen in Sandia National Laboratories' (SNL's) Hypersonic Wind Tunnel (HWT). The remaining two datasets are from simulations of a longer 7° sharp cone at a freestream Mach number of 14, and a flat plate TBL at Mach 14. First, the DNS simulations are introduced (Sect. II), then each is analyzed to characterize its usefulness and the applicability of assumptions related to the ND model (Sect. III). Finally, statistics of the OPD are explained and comparisons are made to expected behaviors (Sect. IV).

Table 1 Flow conditions for the DNS datasets.

	Ma_i	Ma_∞	U_∞ [m/s]	T_∞ [K]	ρ_∞ [kg/m^3]	T_w [K]
Sharp Cone Mach 8	7.9	6.67	1076	61.8	0.075	293
Sharp Cone Mach 14	14.3	10.3	1953	86.8	0.061	296
Flat Plate Mach 8	–	7.87	1155	51.8	0.027	298
Flat Plate Mach 14	–	13.6	1882	47.5	0.017	300

II. Methods

A. DNS data

Four different DNS datasets, all of hypersonic flows, are used here (Table 1). Two of the datasets are the same as the two hypersonic datasets used in Miller et al. [12]. Specifically they are from simulations of a flat plate TBL and of flow over a 7° sharp cone. The flat plate TBL had a Ma_∞ of 7.87 and was previously reported in Zhang et al. [18]. The sharp cone was exposed to an inflow Mach number (Ma_i) of 7.9 based on HWT [19], which resulted in a shock layer Mach number (which was the effective freestream Mach number for the BL) of 6.67. Data from this simulation were also used in Huang et al. [20].

The new DNS datasets include a simulation of flow over a similar 7° sharp cone, but at a new Ma_i of 14.3. After the shock, this results in Ma_∞ = 10.3. The other new dataset is of BL flow over a flat plate with Ma_∞ = 13.6 and is also reported on in Zhang et al. [18].

Multiple competing interests/effects put restrictions on the size of the domain, or the aperture (Ap), that is appropriate for conducting optical analysis of TBLs. First, the interest of this work is only in fully-developed turbulent boundary layers, and therefore data from only near the downstream ends of the DNS domains are used. Next, for the sake of normalizing optical differences by δ, as in Eqn. 6, it is also desirable to have the streamwise extent of the Ap (Ap_x) to be small enough that δ is not changing significantly within that space. In Gordeyev et al. [8], they propose that Ap_x should be kept small enough such that,

$$\frac{0.23 Re_{Ap}}{Re_\delta^{5/4}} << 1, \tag{8}$$

where Re_{Ap} and Re_δ are the Reynolds numbers based on Ap_x and δ, respectively. Keeping the extent this small ensures that there is little bulk variation in boundary layer dynamics across the Ap. However, if the streamwise extent is too small, it is well documented that the distribution of OPDs seen within the Ap will miss structures of some sizes and that the calculated OPD_{rms} will therefore be less than is actually reality for that BL [4, 8]. Thus, while the Ap should be kept small so that BL growth can be neglected, it should not be made smaller than approximately 7δ, or the measured values of OPD_{rms} will be incorrect. Similarly, the spanwise extent of Ap (Ap_z) should not be smaller than approximately 2δ. So, for each of the DNS datasets used here, an appropriately sized Ap was identified near the downstream end of the domain and only data from that Ap were used for determining optical impacts.

1. Sharp Cone BLs

Two DNSs of a 7° half-angle sharp cone were performed using Sandia's Parallel Aero-Reentry Code (SPARC) [21] with inflow conditions defined to match centerline conditions of SNL's HWT and Arnold Engineering Development Complex's (AEDC's) Tunnel 9. Both tunnels are conventional blowdown-to-vacuum tunnels that can be operated at multiple Mach numbers including Mach 8 and 14, and have been used for a variety of experiments of flow over sharp cones (e.g., [22, 23]).

For the Mach 8 cone DNS, the inflow conditions were set to T_i = 46.1 K, ρ_i = 0.038 kg/m^3, and U_i = 1092 m/s following Smith et al. [19]. The simulated working gas was nitrogen, which with these inflow conditions, had an inflow Mach number of Ma_i = 7.9. Although the entire nose was not resolved in the mesh (see [12]), the bow shock was resolved starting at x = 0.2 mm and tracked along the vehicle to the outlet plane. For the sake of scaling the TBL, the needed "freestream" conditions are those that existed in the shock layer (behind the shock but beyond δ). These conditions were T_∞ = 61.8 K, ρ_∞ = 0.075 kg/m^3, U_∞ = 1076 m/s, and Ma_∞ of 6.67. The cone itself was maintained

at a constant isothermal wall temperature of T_w = 293 K.

The full mesh had nearly 3 billion grid cells and resolved a 30° azimuthal slice of the cone. Only a small portion of the whole mesh was utilized in this work. Specifically, the integrations through the boundary layer were performed in the $+y$ (not the wall-normal or cylindrical-radial directions) and an Ap of only 2 × 2 cm was defined near the aft end of the cone [12]. The data from the original mesh were interpolated to a similarly-resolved mesh defined from the cone surface up to just inside the shock. This direction of integration was chosen to match the expected direction that an experimental setup would also be able to collect data in a wind tunnel, i.e., by passing a laser through the cone TBL to or from the tunnel wall (Lynch et al. [15] and Butler et al. [13] have established procedures for such an experiment). Twenty-two independent frames of data were used from this DNS.

The DNS of the sharp cone at Mach 14 was run with nitrogen as the working gas and inflow conditions of T_i = 45.7 K, ρ_i = 0.019 kg/m^3, U_i = 1974 m/s, and Ma_i = 14.3, based on Marineau et al. [23]. This resulted in "freestream" conditions of T_∞ = 86.8 K, ρ_∞ = 0.061 kg/m^3, U_∞ = 1953 m/s, and Ma_∞ = 10.3 behind the shock. This cone was also kept isothermal at T_w = 296 K.

The full mesh resolved a 180° azimuthal angle of the cone (half the full domain) and was composed of over 14 billion grid cells. Again only a small portion was used here with an Ap of 5.1 × 2.9 cm defined near the aft end of the resolved portion of the cone (75.4 < x < 80.5 cm). Again integrations were performed on data that was interpolated to a useful grid oriented in the $+y$ direction from the cone surface and which maintained the Ap cross-section up to just below the shock. A total of 14 independent frames were used to get the optical statistics presented below.

2. Flat Plate BLs

The two hypersonic flows over flat plates were previously reported as the M8Tw048 and M14Tw018 cases in Zhang et al. [18]. Starting with the Mach 8 simulation, the original domain had streamwise (x), wall-normal (y), and spanwise (z) dimensions of 1.3 m (65 times the prescribed δ_i of 20 mm), 41.2δ_i, and 10.2δ_i, respectively. The Ap was defined using only the last 700 cells in the streamwise direction (x > 1.02 m) and the full spanwise extent. Integrations were then conducted from the wall up to y = 8.7 cm, as no identifiable variation in state variables existed farther from the wall. Forty-two individual, statistically-independent density fields were used in the optical analysis. The volume of data used from each field was resolved by 700 × 500 × 310 = 108 million cells.

The flow conditions for this simulation were chosen to be representative of the nozzle exit of SNL's HWT. This equated to a T_∞ of 51.8 K, ρ_∞ of 0.026 kg/m^3, and U_∞ of 1155.1 m/s, which collectively result in a freestream Mach number of 7.87. The wall was treated as isothermal with a temperature of 298 K.

The Mach 14 simulation was originally performed as two simulations on separate domains with a plane near the outflow of the first domain being used as the inlet plane for the second domain [18]. For this work, only the downstream domain is used, and again the domain was cropped to a reasonable Ap and in the wall-normal direction to remove points where no identifiable state changes existed. The Ap was defined using only the last 550 of the 2000 points in the streamwise direction and the full spanwise extent of the domain. These crops resulted in physical dimensions of 3.60 < x < 4.13 m, z = 22.0 cm, and y < 16.7 cm. This volume was resolved with 550 × 460 × 430 = 109 million cells and a total of 28 independent density fields were used for the optical analysis.

Conditions from the AEDC Hypervelocity Tunnel No. 9 were used as the flow conditions for the Mach 14 simulation. For the portion of the domain used here, this resulted in effective freestream conditions of T_∞ = 47.5 K, ρ_∞ = 0.0172 kg/m^3, and U_∞ = 1881.9 m/s, which collectively make Ma_∞ = 13.6. The wall was isothermal at T_w = 300 K.

B. Refraction index and BL scales

Each frame of density from each DNS dataset was used to calculate the refraction index via Eqn. 2. The refraction-index fields were then numerically integrated via a trapezoid rule from the wall into the freestream following Eqn. 1. This method essentially treats each column of data within the mesh (oriented in the $+y$) as an individual ray path. Different resolutions of streamwise and spanwise sampling were done to test whether localized correlation within the flow would bias the results, but given the number of independent snapshots used, this was found to never be a problem.

The integrations produced OPLs for every point within the defined Ap. Equation 3 was then used to remove the mean OPL and tilt for each frame to get fields of OPD. The OPD_{rms} was then defined as based on the distribution of OPD values across the spanwise and streamwise extents of the Ap. Variations in OPD_{rms} across the independent frames of data were used to define the uncertainty bands shown in figures later.

In addition to determining OPD_{rms} for each flow, the boundary layer thicknesses and coefficients of friction were determined directly from the DNS data for use in comparing to models. The boundary layer thickness was determined

using thresholds in the mean streamwise total enthalpy, h_0.

III. DNS characterization

Each of the DNS datasets was investigated to check for sufficient convergence of the turbulent statistics as well as to ensure that all of the relevant scales were in expected ranges. Additionally, as part of the derivation of the ND model, as presented in Eqn. 6, multiple assumptions are made that allow for the behavior of the local fluctuating density field to be approximated via mean profiles which are integrated as part of F. The validity of these assumptions is checked for each of the DNS datasets prior to then making final comparisons of the ND model to the OPD_{rms} values calculated directly from the index of refraction fields.

First, as part of the ND model it is assumed that the profile of the root-mean-square of the density can be approximated with the profile of the root-mean-square of the temperature as,

$$\frac{\rho'_{rms}(y)}{\overline{\rho}(y)} = \frac{T'_{rms}(y)}{\overline{T}(y)}, \tag{9}$$

and thus that pressure fluctuations are negligible. The validity of this assumption is demonstrated for each of the DNS datasets by comparing the profiles of $\rho'_{rms}(y)/\overline{\rho}(y)$ and $T'_{rms}(y)/\overline{T}(y)$.

Second, it is also assumed that fluctuations in the temperature can be approximated with fluctuations in the velocity via adiabatic heating. This is known as the Strong Reynolds Analogy (SRA), the averaged form of which is,

$$T'_{rms}(y) = \frac{A(y)\overline{U}(y)u'_{rms}(y)}{c_p}, \tag{10}$$

where c_p is the specific heat of the working fluid at constant pressure and $A(y)$ includes an integral of the stress and is ≈ 1.0 for most of the BL [11, 24]. This form of the SRA inherently assumes that the flow is over an adiabatic wall, and that there is a perfect anti-correlation between fluctuations in the velocity and in the temperature everywhere in the BL. Given that the datasets used here are all from simulations with isothermal (cooled) walls, an extended form of the SRA (an ESRA) is used instead of Eqn. 10. One of the simplest derivations of an ESRA comes by assuming a linearization of the Walz equation, with $\partial T/\partial U \approx T'/u'$, and then applying the root-mean-squared operator. This results in an ESRA of,

$$T'_{rms}(y) = u'_{rms}(y)\left(\frac{A(y)\overline{U}(y)}{c_p} - \frac{T_r - T_w}{U_\infty}\right), \tag{11}$$

where T_r is the recovery (adiabatic) wall temperature defined as,

$$T_r = T_e + r\frac{U_e^2}{2}\frac{\gamma - 1}{\gamma R}, \tag{12}$$

γ is the ratio of the specific heats, and the subscripts "e" and "w" represent edge and wall quantities, respectively. For each of the datasets, the applicability (or lack thereof) of the ESRA is demonstrated by comparing the left- and right-hand sides of Eqn. 11. For all of the results reported here, $A(y)$ was approximated with $A(y/\delta) = 7/4 - 1/((5/4)(y/\delta)^4 + 4/3)$ [12].

While both of these assumptions have been shown to work well for flows up to Mach 3 ([25] among others), they clearly introduce problems for hypersonic flows and/or for datasets with non-adiabatic walls. In Miller et al. [12], the validity of the assumptions was again demonstrated for a subsonic and supersonic TBL. While the assumptions were not as clearly valid for the hypersonic datasets presented therein, the final results for the ND model still appeared reasonable.

A. Sharp Cone BLs

1. Mach 8

The BL edge was identified as the location of the maximum overshoot in the total enthalpy profile and led to $\delta = 4.1$ mm. Because $Ap = 2$ cm square, $Ap/\delta = 4.9$ in both the streamwise and spanwise direction. This is below the desired value for the streamwise direction in order to not need to correct for small-aperture effects, but is higher than the needed value for the spanwise [4]. No correction has been made at this time. The Reynolds ratio, $0.23Re_{Ap}/Re_\delta^{1.25}$ is 0.068

Table 2 Relevant BL properties from the DNS datasets taken as means over the apertures. Both the compressible and *incompressible* equivalents for Re_θ and C_f are shown.

	δ [mm]	θ [mm]	U_e [m/s]	ρ_e [kg/m^3]	Ma_e	T_w/T_r	Re_θ	C_f
Sharp Cone Mach 8	4.1	0.14	1071	0.070	6.33	0.511	2695(*747*)	1.4e-3(*4.8e-3*)
Sharp Cone Mach 14	5.6	0.17	1933	0.050	8.70	0.165	3353(*1494*)	9.8e-4(*4.1e-3*)
Flat Plate Mach 8	39.0	1.2	1151	0.023	7.34	0.465	9471(*2214*)	8.5e-4(*3.7e-3*)
Flat Plate Mach 14	68.2	1.4	1864	0.012	10.7	0.184	14566(*4077*)	5.8e-4(*3.1e-3*)

and thus small enough to ignore mean BL growth over the aperture [8]. A variety of other BL edge quantities were also identified and are listed in Table 2.

The compressible momentum thickness (θ) was determined via integration of the mean velocity profile taken from across the Ap and was used to determine the compressible Re_θ which is 2695. This was converted to an incompressible equivalent following an approach typically used for isothermal flat plates. Given the relatively narrow Ap and the fact that profiles were defined in the $+y$ direction instead of the radial direction, it was decided that no alteration to account for the cone geometry was warranted. The isothermal flat plate approach to incompressible equivalency is defined as,

$$Re_{\theta,incomp} = Re_\theta \frac{\mu_e}{\mu_w}, \tag{13}$$

and results in a value of 747 [26]. This definition is different than was used in Miller et al. [12] and by others (e.g., [27]), wherein μ_∞ was used in place of μ_e. For high Mach number flows, the gradient in the temperature is relatively steep near the BL edge. And as the Mach number increases, that gradient also steepens at $y = \delta$. This means that if the identification of δ is done correctly, it will likely lead to μ_e differing considerably from μ_∞ and an incorrect equivalency will result if μ_∞ is used instead of μ_e. For this case, with $Ma_\infty = 6.67$, $\mu_e \approx \mu_\infty$ and thus the difference in definition is of little consequence. At Mach 14, however, μ_e differs more significantly from μ_∞ and if μ_∞ were to be used an incorrect equivalency would result in the next section.

The friction coefficient was determined based on its definition using data from the first cell off the wall from the mean velocity profile. It has a value of 1.4e-3 but was then also converted to an incompressible equivalent following the Van Driest approach [28]. Because the simulation was performed with an isothermal wall the approach is,

$$C_{f,incomp} = C_f F \tag{14}$$

where,

$$F = \frac{T_r/T_e - 1}{(\mathrm{asin}(A) + \mathrm{asin}(B))^2}, \tag{15}$$

$$A = \frac{2a^2 - b}{Q}, \quad B = \frac{b}{Q}, \quad a^2 = r\frac{\gamma - 1}{2}\frac{T_e}{T_w}Ma_e^2, \quad b = \frac{T_r}{T_w} - 1, \quad Q = \sqrt{b^2 + 4a^2}, \tag{16}$$

and where the recovery factor, r, was set at 0.896 [24, 28]. This results in an incompressible equivalent C_f value of 4.8e-3.

These two incompressible-equivalent scales are compared to flat plate theory in Fig. 1 via the model predictions of Kármán–Schoenherr,

$$C_f = \frac{1}{17.08(\log_{10}Re_\theta)^2 + 25.11\log_{10}Re_\theta + 6.012}, \tag{17}$$

and of Blasius,

$$C_f = \frac{0.026}{Re_\theta^{1/4}}, \tag{18}$$

[29]. The determined values suggest that each of the datasets used here exemplify a fully developed TBL and that the scaling procedures used should be applicable.

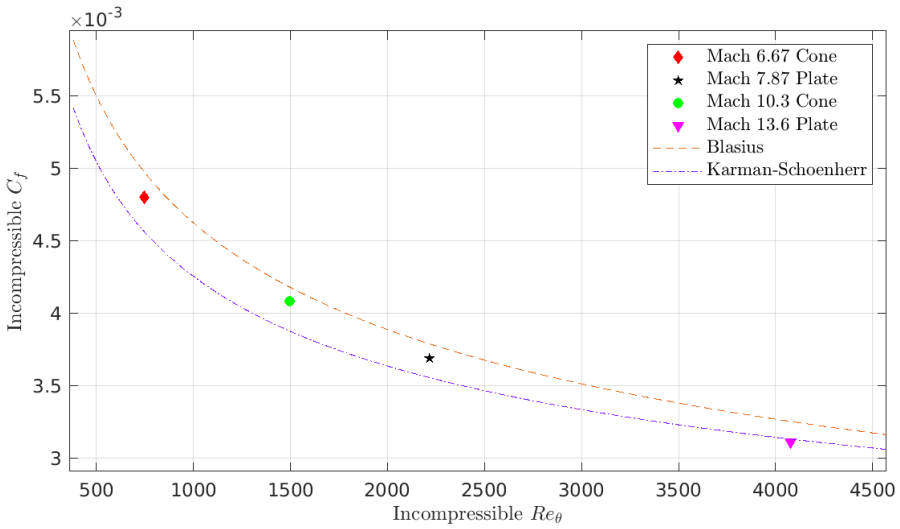

Fig. 1 The incompressible equivalent Reynolds numbers and friction coefficients for each of the studied datasets.

Next, the assumptions related to the substitutions made as part of the derivation of the ND model are tested. Figure 2 shows the profiles of the left- and right-hand sides of Eqn. 9 for each of the DNS datasets. Also depicted are the profiles of $P'_{rms}(y)/\overline{P}(y)$ which were neglected as part of that equation. As can be seen for each of the depicted cases, the profiles of the density and temperature fluctuations do not match each other as well as has been seen at lower Mach numbers [12]. For this Mach 8 cone case specifically, the use of Eqn. 9 has errors of over 40% both near the wall and near $y = \delta$. Additionally, although the pressure fluctuations are significantly less substantial than the fluctuations of density and temperature, they are not zero as assumed. However, they also do not take a shape that would account for the difference in the density and temperature fluctuation profiles, i.e., if $P'_{rms}/\overline{P}$ were to be included in Eqn. 9 as in Gordeyev et al. [11], it would not close the gap between $\rho'_{rms}/\overline{\rho}$ and $T'_{rms}/\overline{T}$. Interestingly however, when the profiles of $\rho'_{rms}/\overline{\rho}$ and $T'_{rms}/\overline{T}$ are integrated from the wall to $y = 1.5\delta$, the difference between them is <1%. So even though the profiles do not exactly match, it may be that using the profile of $T'_{rms}/\overline{T}$ to approximate the profile of $\rho'_{rms}/\overline{\rho}$ may not introduce much error in an integral like that used in the definition of F (see [7]).

Finally, Figure 3 depicts the profiles of the left- and right-hand sides of the ESRA (Eqn. 11) for each of the datasets. For each of the cases, it can be seen that the right-hand side does a decent job of tracking the general shape of the T'_{rms} profiles, but it over-predicts everywhere except right at the wall where it always erroneously predicts a negative value. This is obviously impossible for a root mean square. For the Mach 8 cone case specifically, the ESRA over-predicts T'_{rms} by approximately 10% for nearly the entire BL (ignoring the issues near the wall). Given that this is the case with the lowest Ma_∞, this is smallest error seen from any of the cases studied here. Miller et al. [12] explained that much of this problem is caused by the assumption of the ESRA that velocity and temperature fluctuations must be perfectly anti-correlated, i.e., that the correlation coefficient, R_{uT}, is always -1. In reality, they are not perfectly anti-correlated over the BL thickness and are, in fact, highly positively correlated near the wall in a cooled wall BL [30, 31]. By simply multiplying the right hand side of the ESRA by a more realistic profile of R_{uT}, as a simple correction factor instead of just keeping the assumed profile of $R_{uT}(y) = -1$, the fit of the ESRA is significantly improved, especially near the wall.

Using the DNS data, R_{uT} was calculated for both of the cone cases (Fig. 4). Other than in the lowest 12% of the BL and beyond $y = 1.2\delta$, the two are nearly identical. In that lowest portion both show similar shapes but cross $R_{uT} = 0$ and reach their peak anti-correlation values at different wall-normal location. Duan et al. [30] argued that for cooled-wall TBLs, R_{uT} should go to zero at the wall-normal location of the peak in the mean temperature profile, and that is perfectly corroborated here. The profile shapes found here do differ somewhat from previously reported results for supersonic TBLs (e.g., [30, 31]) in that R_{uT} seems to nearly-linearly trend from its maximum negative value towards zero at $y = 1.3\delta$. Guarini et al. [32] showed profiles that also went to zero at $y = \delta$, but which were relatively flat at $R_{uT} \approx -0.6$ for most of the TBL. It may be that these differences are based on the higher Mach numbers studied here, or differences in the Reynolds number, or on the fact that these data came from a cone simulation instead of a flat plate.

For the cone cases here, these profiles of R_{uT} were multiplied by the right-hand side of the ESRA to test whether this improved the fits, and the resulting curves are also shown in Fig. 4. As can be seen for this Mach 8 cone case, the fit

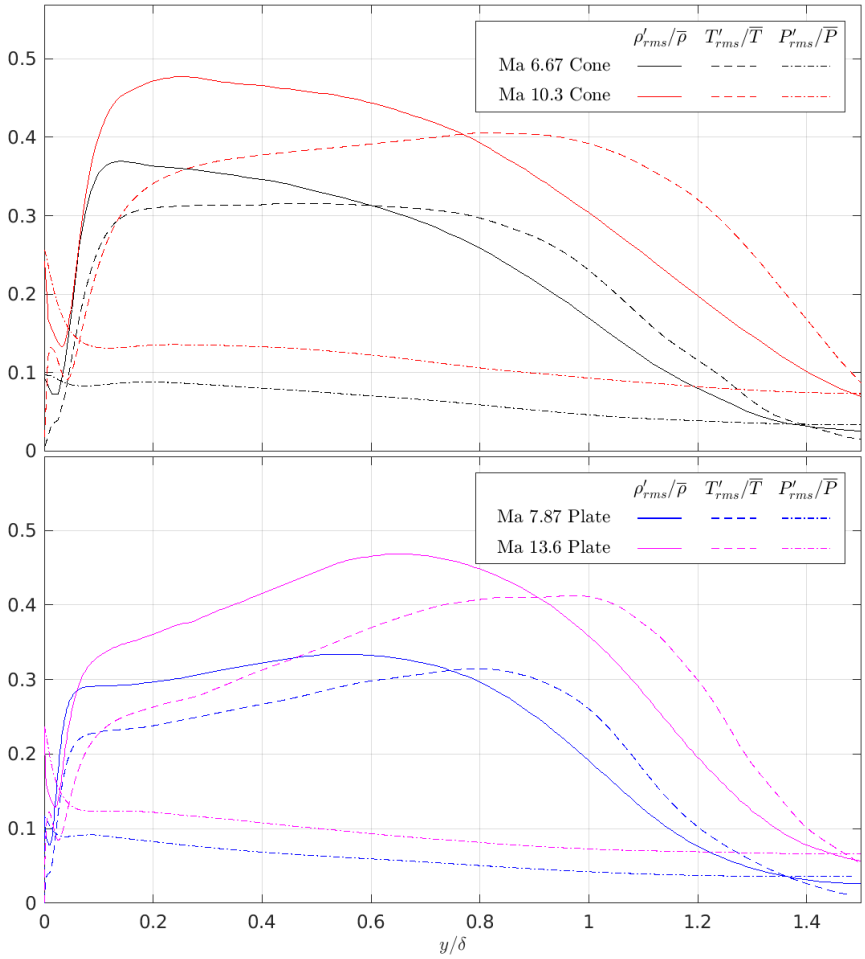

Fig. 2 The aperture-averaged fluctuations of the density, temperature, and pressure as in Eqn. 9.

is improved near the wall and near the peak, but then tends to under-predict T_{rms} for much of the BL thickness. This is obviously undesirable, and for this case specifically, it actually increases the error in the integrals of the respective profiles. It may be that some compromise value of R_{uT}, between what is calculated here and what is assumed by the ESRA (-1), would be more helpful for the outer portions of the BL. In Miller et al. [12] a piecewise linear profile of R_{uT}, that maintained a value of -0.8 for much of the BL, was proposed and did produce a slightly better fit in the outer portions of the BL.

2. Mach 14

The BL edge was again identified based on the total enthalpy profile but this time using the first occurrence at which the profile reached 99.7% of the freestream value as the threshold. This resulted in δ = 5.6 mm which then led to the edge quantities listed in Table 2. The Ap_x was 5.1 cm, leading to Ap_x/δ = 9.1 and $0.23Re_{Ap}/Re_\delta^{1.25}$ = 0.12. While the aperture ratio is definitely large enough so as to negate the need for small-aperture corrections, it may be larger than is desirable and some impact of the BL growth within the aperture may exist in the optical response. Looking at the growth of the BL across the aperture reveals a mean growth from approximately 5.0 to 6.4 mm. Although Miller et al. [12] demonstrated how accounting for streamwise variation can be performed when quantifying optical distortions, for this work, no accounting for this growth was made. In future works the aperture will likely be trimmed to more optimally fit the desired ratio thresholds.

The momentum thickness was determined to be 0.17 mm which led to the compressible Re_θ being 3353 which converted to an incompressible equivalent of 1494. The compressible coefficient of friction was found to be 9.8e-4,

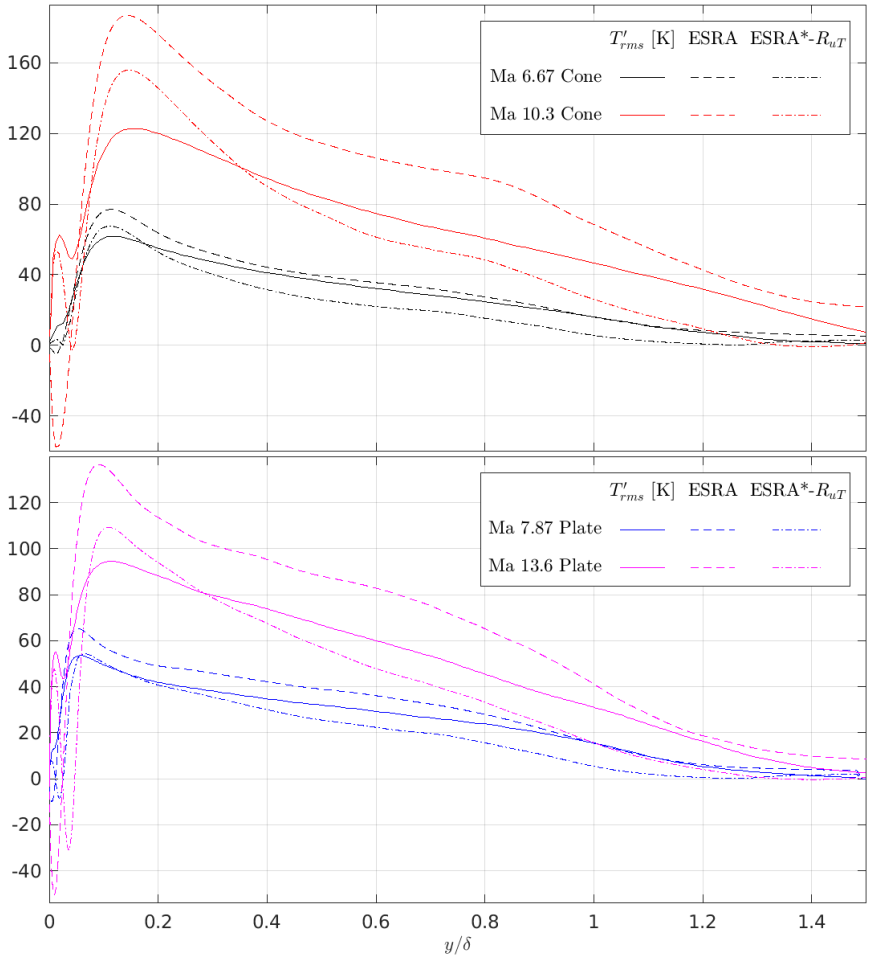

Fig. 3 The aperture-averaged left- and right-hand sides of Eqn. 11.

which converted to an incompressible equivalent of 4.1e-3, thus demonstrating that this is a well developed TBL and that scaling variables should be reliable for normalization of the optical behaviors (Fig. 1).

The fluctuating state variable profiles for this case follow very similar shapes as for the Mach 8 cone flow but with higher magnitudes across the studied space (Fig. 2). Again the profile of $T'_{rms}/\overline{T}$ is not a perfect approximation of $\rho'_{rms}/\overline{\rho}$, with errors of 27% near the peak ($y = 0.2\delta$) and 72% just outside the BL, but the integrals of the two profiles return quite similar values. Specifically, the integrals of $T'_{rms}/\overline{T}$ and $\rho'_{rms}/\overline{\rho}$ from the wall up to $y = 1.5\delta$ differ by 1.8%.

The profiles of T'_{rms} and the right-hand side of the ESRA are again shown in Fig. 3, along with the version of the ESRA profile that is multiplied by the negative of the Mach 14 R_{uT} profile in Fig. 4. As with the Mach 8 cone data, the ESRA over-predicts the T'_{rms} profile everywhere except near the wall, with errors averaging 45% for $0.07 < y/\delta < 1.35$. When the correction is made using the correlation coefficient, the behavior near the wall and near the peak are again improved but the corrected ESRA now tends to under-predict T'_{rms} for $y > 0.35\delta$. This is still a general improvement, however, and brings the relative errors to within 20% for most of the BL thickness, and reduces the differences in the integrals (over $0 < y < 1.5\delta$) from a 39% over-prediction for the ESRA to a <15% under-prediction for the corrected version. Again, a compromised version of the R_{uT} that took a value of perhaps -0.6 for the outer half of the BL and beyond, may be a better correction.

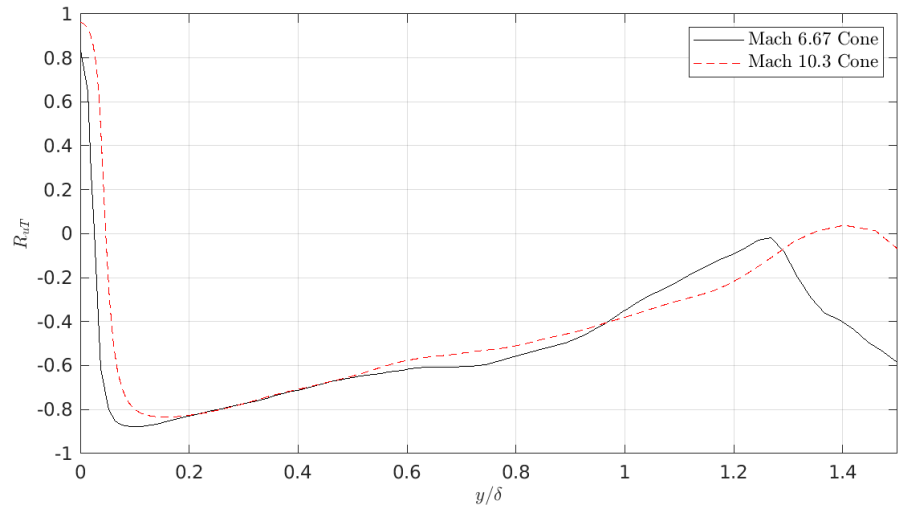

Fig. 4 The correlation coefficient between u' and T' as a function of wall-normal distance.

B. Flat Plate BLs

1. Mach 8

The BL edge was identified as the location where the total enthalpy profile reached its maximum overshoot. δ grew over Ap_x from 3.6 to 4.1 cm with a mean of 3.9 cm. Given that Ap_x was 28.4 cm, this resulted in a mean streamwise Ap/δ ratio of 7.3, and thus Ap_x was large enough that small-aperture corrections were not necessary or applied [4, 8]. Additionally, by using the mean δ, $0.23Re_{Ap}/Re_{\delta}^{1.25}$ = 0.071, and thus the requirement that Ap_x be small enough to neglect mean BL growth was also satisfied.

The compressible momentum thickness was determined and led to a compressible Re_θ of 9471. This was converted to its incompressible equivalent which resulted in a value of 2214. The compressible friction coefficient was determined to be 8.5e-4 but was then also converted to its incompressible equivalent. This resulted in an incompressible value of 3.7e-3 (Fig. 1).

With respect to the profiles of the fluctuating state variables, for the flat plate flows there is an obvious difference in the overall shape when compared to the cone BLs (Fig. 2). While the peaks in the $\rho'_{rms}/\overline{\rho}$ profiles tend to occur at around y/δ = 0.2 for the cones, the peaks are in the outer half of the BL for the flat plates. Additionally, for the profiles of $T'_{rms}/\overline{T}$, while they are relatively flat for much of the cone BLs, the flat plate profiles exhibit a more distinctive peak, again in the outer portions of the BL. As a demonstration of what leads to this, two-dimensional slices of the wall-normal gradient of the density are shown for representative planes through individual snapshots of the two flat plate DNS datasets (Fig. 5). As can be seen, the most extreme local density fluctuations are spread over a larger wall-normal extent centered near the middle of the BL for the Mach 8 case and are clustered closer together and closer to $y = \delta$ for the Mach 14 case. It is documented that as the Mach number increases, while keeping the wall cooling rate constant, that the location of the peaks of the relative density and temperature fluctuations tends to move towards the BL edge [18]. Alternatively, when the Mach number is kept constant and the wall cooling is increased, fluctuations tend to be dampened and a clear peak is less likely to materialize [30]. Within both the cone datasets and the flat plate datasets, the increase in Mach number tends to move the peak farther from the wall, but this effect does not explain the differences seen in the shapes between the profiles from the different geometries (cone vs flat plate). Taken collectively, the four datasets do not create a trend in the peaks that is fully supported by these explanations. It is possible that the differences can be explained by the spanwise curvature of the cone or perhaps by the differences in the Reynolds numbers but no further speculation is made here.

The relative difference between the profiles of $\rho'_{rms}/\overline{\rho}$ and $T'_{rms}/\overline{T}$ for the Mach 8 flat plate is approximately 20% for much of the lower half of the BL and reaches a maximum error of 42% at y/δ = 1.1—ignoring the extreme errors very near the wall and farfield errors where T'_{rms} goes to zero (Fig. 2). The integrals of the two profiles were performed over the depicted range and the result is that the $T'_{rms}/\overline{T}$ profile is a 4.4% under-prediction of the integral of the $\rho'_{rms}/\overline{\rho}$ profile. This is an increase over both of the cone cases and suggests that even if the ESRA is a perfect approximation of

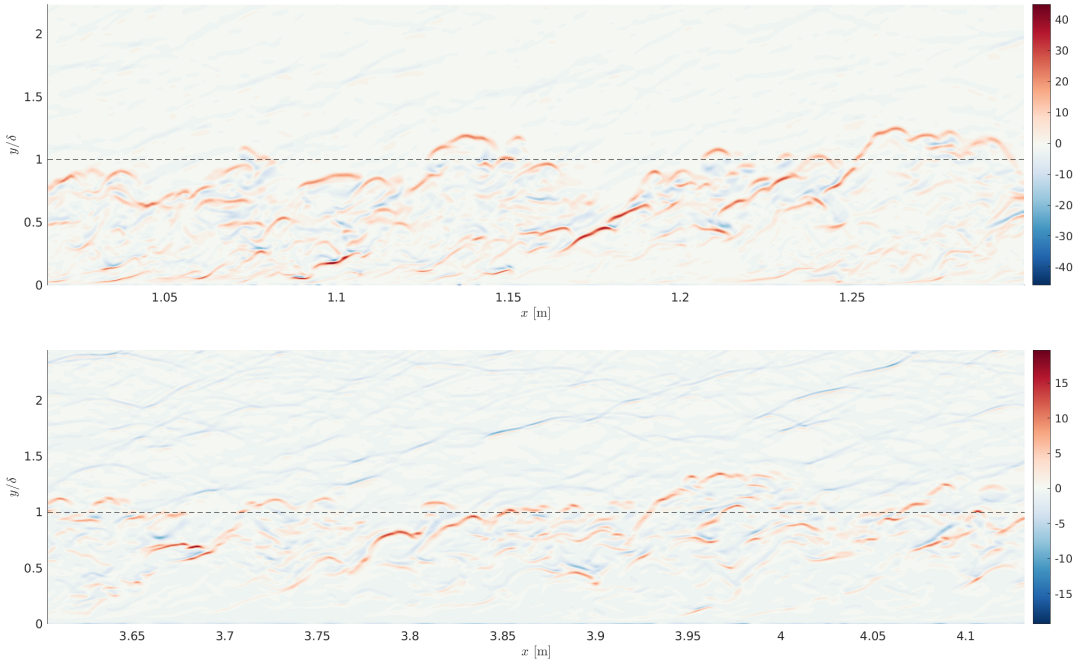

Fig. 5 Two-dimensional slices of the wall-normal density gradient in [kg/m^4] for the Mach 8 (top) and Mach 14 (bottom) flat plate TBLs.

$T'_{rms}/\overline{T}$, error is still propagating to the ND model estimate.

As was seen with the cone cases, the normal ESRA tends to over-predict T'_{rms} basically everywhere in the BL for the Mach 8 flat plate case (Fig. 3). Specifically, it over-predicts by about 20% nearly everywhere below $y = 0.8\delta$, including at the peak (at $y/\delta = 0.05$). Because a profile of R_{uT} was not available for this dataset specifically, the profile from the Mach 8 cone as used and multiplied by the ESRA to produce the corrected version. This approach has obvious flaws associated with it, not the least of which is the fact that the peaks in the profiles of T'_{rms} occur at different distances from the wall, and thus the profiles of T'_{rms} from the flat plate and R_{uT} from the cone are not appropriately aligned. Regardless of this, the corrected ESRA appears to be a significant improvement over the ESRA right at the peak in the T'_{rms} profile. Unfortunately, as was the case with the Mach 8 cone, it then under-predicts T'_{rms} for the majority of the rest of the depicted range. It is likely that the actual profile of R_{uT} for the Mach 8 flat plate would be shaped more like those reported for a Mach 5 cooled flat plate in Duan et al. [30] and that using a profile of that shape would prevent the under-prediction seen here. This was done in Miller et al. [12] using an assumed piecewise linear profile and a superior prediction was produced.

Interestingly, given that the integral of the profile of $T'_{rms}/\overline{T}$ is an under-prediction of the integral of $\rho'_{rms}/\overline{\rho}$ by 4.4%, the over-prediction of T'_{rms} by the ESRA actually works to cancel that error out when both substitutions are made. The integral of the ESRA profile is an over-prediction of the integral of T'_{rms} by 18%. When the ESRA is divided by $\overline{T}(y)$ and the resulting integral is compared to the integral of $\rho'_{rms}/\overline{\rho}$ the difference is still 13%. Because the corrected ESRA under-predicts T'_{rms}, when this same calculation is done the errors actually compound to make the prediction of the integral of $\rho'_{rms}/\overline{\rho}$ worse.

2. Mach 14

As was done for the Mach 14 cone, a threshold of 99.7% of the freestream total enthalpy was used to determined δ. This resulted in a mean value of $\delta = 6.8$ cm over Ap. The aperture for this case was 52.7 cm in the streamwise direction, resulting in $Ap_x/\delta = 7.7$ and $0.23Re_{Ap}/Re_\delta^{1.25} = 0.061$, thus perfectly satisfying both of the Ap size requirements described above.

The momentum thickness and Re_θ were then 1.4 mm and 14566, respectively, and the incompressible equivalent Re_θ was 4077 (determined using μ_e). The compressible friction coefficient was 5.8e-4 and the incompressible equivalent

was 3.1e-3 (Fig. 1).

The profiles of the state variable fluctuations show that the magnitudes of all three variables have increased compared to the Mach 8 case (Fig. 2). Additionally, the peaks in $\rho'_{rms}/\overline{\rho}$ and $T'_{rms}/\overline{T}$ have moved farther away from the wall than in the Mach 8 case, as discussed. The peak in the fluctuations of $\rho/\overline{\rho}$ now occurs at y/δ = 0.7 while the peak in the fluctuations of $T/\overline{T}$ now occur right at the BL edge. Because the index of refraction is linearly related to the local densities, it would then be expected that the largest contributions to optical distortions would occur in the outer portions of the BL (again see Fig. 5).

The relative difference between $\rho'_{rms}/\overline{\rho}$ and $T'_{rms}/\overline{T}$ also increased in going from Mach 8 to 14. Much of the lower portions of the BL now exhibit differences of about 25% while the maximum error is 56% at y/δ = 1.25. Integrals of the two profiles revealed that the profile of $T'_{rms}/\overline{T}$ is a cumulative under-prediction of the profile of $\rho'_{rms}/\overline{\rho}$ by 8.6%.

The ESRA profiles are compared for the Mach 14 case in Fig. 3 and show similar behavior as was seen for Mach 8. Specifically, the right-hand side of the normal ESRA over-predicts the temperature fluctuations everywhere in the BL, except at the wall where it predicts the incorrect sign and profile shape. By using R_{uT} taken from the Mach 14 cone case, as the correction to the ESRA, a significant improvement in the prediction of the T'_{rms} is observed near the wall and near the peak. However, in the space between $0.02 < y/\delta < 0.05$, because of the misalignment of the T profile from the cone and the T profile from the flat plate, the use of the cone correlation profile results in some negative values coming from the corrected ESRA. This is one of the things meant to be fixed by using real profiles of R_{uT}, but obviously was not fixed by using the profile from the other case. Regardless, this version of the corrected ESRA is still a general improvement over the nominal version. While the ESRA produces relative prediction errors of nearly 50% for much of the BL, the corrected version maintains relative errors of <20% for most of the BL. By integrating the three profiles and comparing, the ESRA over-predicts by 31%, and that is even with the large erroneous negative region near the wall helping to cancel some of the general over-prediction in the rest of the BL. The integral of the corrected ESRA was only 19% lower than the integral of $T'_{rms}(y)$.

IV. Aero-optics Characterization

While deeper investigations into the effects of wall-cooling will occur in the future, herein we have chosen to forgo attempting to quantify the specific effects of the wall cooling and stick purely with comparisons of the data to Eqn. 6. This decision is warranted, somewhat, by the finding in Gordeyev et al. [11] that the impact of wall cooling on the OPD_{rms} can be quantified as a function of $\Delta T/(T_\infty Ma_\infty^2)$. For the datasets studied here, the expected alteration in the OPD_{rms} from the wall cooling is <10%.

A. Sharp Cone BLs

The OPD_{rms} value found for the BL over the sharp cone in the Mach 8 inflow was 9.15 nm with a 95% confidence interval (between the 2.5 and 97.5 percentiles) of all the individual OPD values spanning from -17.9 to 17.9 nm. As explained, Gordeyev et al. [11] showed that the impact on OPD_{rms} from wall cooling can be predicted as a function of $\Delta T/(T_\infty Ma_\infty^2)$. For this flow, $\Delta T/(T_\infty Ma_\infty^2) = -0.10$ with Ma_∞ = 6.67 which means that the OPD_{rms} of 9.15 nm reported here is likely lower, by about 10%, than the OPD_{rms} that would be found for an otherwise identical adiabatic simulation. Thus, Eqn. 6 is not expected to be directly applicable for this case and would perhaps be expected to predict an OPD_{rms} value of over 10 nm when used as a model. Why then is the model line lower than the OPD_{rms} determined here? First, the model line is showing F not OPD_{rms} directly, and second, it is unknown how the other relevant scales of the normalization (e.g., C_f, δ) would also be altered in an otherwise identical adiabatic simulation. Early results suggest that for an adiabatic TBL, although OPD_{rms} may be higher, changes in the other variables may in fact result in F being lower. The ongoing work of Castillo et al. [14] is setting up the capability to be able to investigate the impact of wall cooling on the OPDs and scaling variables in hypersonic TBLs using Large-Eddy Simulation (LES). If these early findings happen to be correct, that may explain why the cooled wall point determined here is higher than the model line in Fig. 6. It is also possible that other effects, like the spanwise curvature of the cone or the fact that the integration was performed at a 7° tilt from the wall-normal may also contribute to this difference [4, 8]. Regardless, only the nominal value of 9.15 nm is used for now and the direct comparison is shown. Using Eqn. 6, a mean value for F of 0.078 was computed with variations across the ensemble of individual frames spanning a 95% confidence interval from 0.067 to 0.090, shown as the errorbars in the figure.

For the cone with the Mach 14 inflow the OPD_{rms} was found to be 13.3 nm with a 95% confidence interval spanning -26.4 to 26.3 nm. $\Delta T/(T_\infty Ma_\infty^2)$ was -0.16 which suggests that this case is closer than in the Mach 8 case to the value at which the largest reduction of OPD_{rms} is likely (-0.4, see [11]). However, the higher value of Ma_∞ means that the

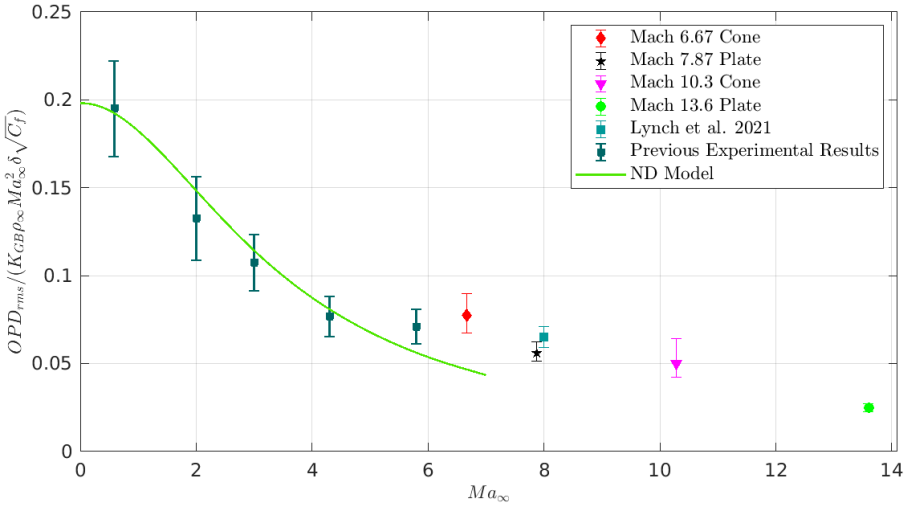

Fig. 6 The normalized OPD_{rms} values from the DNS datasets along with data from previous experiments reported in Gordeyev et al. [17] and Lynch et al. [15]. The ND model is also shown to Mach 7 [5].

reduction compared to an adiabatic case is still likely of a lower total percentage than in the Mach 8 case, i.e., this case is likely seeing a reduction compared to the adiabatic OPD_{rms} of only a few percent. The calculated value of 13.3 nm was used along with the other BL scales to determine F to be 0.050 with a 95% confidence interval span, based on the individual frames used in the ensemble, of 0.042 to 0.064 (Fig. 6).

B. Flat Plate BLs

The OPD_{rms} value taken across all of the data from the ensemble of frames for the Mach 8 flat plate case was 24.5 nm, with a 95% confidence interval of the individual OPD values spanning from -49.0 to 46.8 nm. $\Delta T/(T_\infty Ma_\infty^2)$ was -0.11, so again these OPDs are likely only a few percent lower than would be expected for an otherwise identical adiabatic TBL. Following Eqn. 6, F then takes a value of 0.056 with a confidence interval based on the individual frames of the ensemble spanning from 0.051 to 0.062 (Fig. 6). This distribution is slightly lower than, but has considerable crossover with, the values reported in Lynch et al. [15] which were collected experimentally on the wall of SNL's HWT.

The OPD_{rms} value for the Mach 14 flat plate BL is 30.2 nm with a 95% confidence span of the individual OPD values of -58.5 to 60.3 nm. $\Delta T/(T_\infty Ma_\infty^2)$ is -0.15 and thus the 30.2 nm found for this case is likely only a few percent below what would be seen for a similar adiabatic TBL. The ND model function value, F, is then 0.025 with a confidence interval based on the ensemble of individual frames spanning from 0.023 to 0.027.

C. Cumulative contribution to OPD_{rms}

In addition to calculating the total OPD_{rms}, the contributions to that total as a cumulative function of the wall-normal distance were also calculated. This was done by integrating Eqn. 1 from the wall up to each individual wall-normal grid location, calculating the resulting OPD field, and then getting OPD_{rms} at each of those locations. The final OPD_{rms} value in each case is then the value being used for Fig. 6. Wang and Wang [4] performed this same analysis for the cases studied therein. Figure 7 shows the accumulation of the OPD_{rms} for each of the cases as a cumulative density function (CDF).

Generally speaking, as the Mach number increases, less and less relative contribution to the total OPD_{rms} was observed in lower portions of the BL, i.e., for any wall-normal location between 0.12δ and 1.0δ the percent contribution to the total OPD_{rms} was smaller for each subsequently higher Ma_∞. For example, at the BL mid-height ($y = 0.5\delta$), the four datasets, in order of increasing Mach number, show that 41%, 32%, 30%, and 19% of the totals can be accounted for, respectively. At the edge of the BL, the cumulative contributions are 88%, 87%, 74%, and 68%, respectively, meaning that the rest of the total OPD_{rms} comes from fluctuations happening intermittently above δ, or from fluctuations radiated by the TBL into the freestream. Figure 5 shows the existence of both of these contributors with individual structures

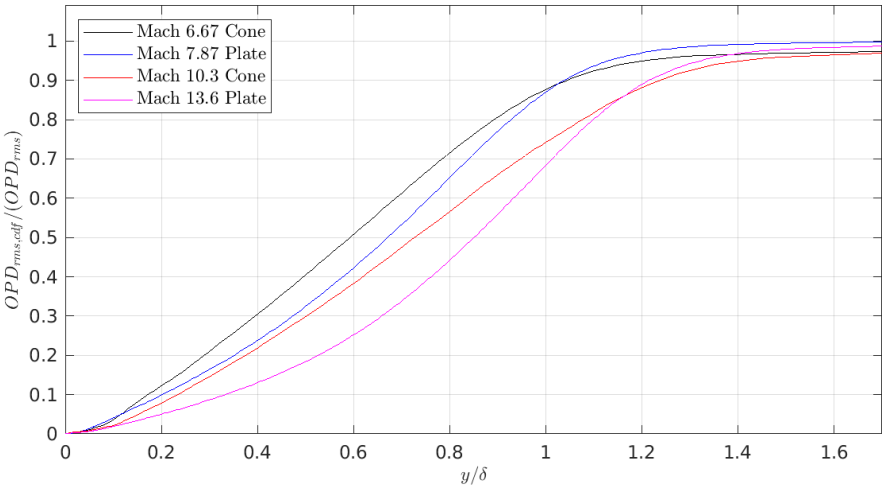

Fig. 7 The relative contribution to the total OPD_{rms} as a function of the wall-normal distance from all locations from the wall to that wall-normal location.

reaching beyond δ and with freestream fluctuations which are stronger in the Mach 14 case than in the Mach 8.

This change in contribution per wall-normal distance as a function Mach number can also be tied to the behavior of the profiles of $\rho'_{rms}/\overline{\rho}$ and where their peaks land. As discussed previously regarding Fig. 2, as the Mach number increases the profiles tend to fill out a larger portion of the BL thickness and the peaks tend to move outward, thus suggesting that a larger contribution to the optical distortions will occur farther from the wall. Note also that the differences in the shapes of the $\rho'_{rms}/\overline{\rho}$ profiles from the cone cases to the flat plate cases is likely tied to the differences in the shapes of the CDFs in Fig. 7. The flat plate cases showed much more distinctive peaks in $\rho'_{rms}/\overline{\rho}$ in the outer BL, and here those same cases show steeper increases in OPD_{rms} at those same wall-normal locations. The cone cases had much flatter profiles of $\rho'_{rms}/\overline{\rho}$, and here they show that the OPD_{rms} tends to grow relatively linearly through most of the BL.

V. Conclusions and Future Work

In this work we have extended the understanding of turbulence-induced Optical Path Distortions to Mach numbers for which the OPD has never before been studied. While Wyckham and Smits [9], Miller et al. [12], and Lynch et al. [15] have previously discussed OPD behavior up to Mach 8 TBLs, never has Mach 14 data been studied in this way. In addition to reporting OPD_{rms} values, we attempted to demonstrate other mean behaviors of hypersonic TBLs that are likely of importance to the behavior of OPDs and that need to be understood prior to deriving a more unified model for OPD_{rms} for hypersonic and non-adiabatic flows. Specifically we investigated the applicability of using fluctuations in temperature as a substitute for fluctuations in density and the applicability of the ESRA as a way to approximate fluctuations in temperature. While both of these equations showed generally the correct trends within the boundary layer, both exhibit clear inaccuracies. Interestingly, these inaccuracies tend to counter-balance each other somewhat and the ND model derived by assuming both of them still seems to perform reasonably well into the hypersonic regime.

These findings clearly motivate future development of the ND model that could extend its usability into hypersonic BLs. Extrapolation of the model could be done via the assumption that the requisite profiles are self similar across the Mach range of interest but with the expectation that the accuracy would decrease as the extrapolation is extended farther from available truth data. Alternatively, the explicit use of real profiles and an interpolation of the model behavior across that regime should produce better model approximations, but this would require new data at the desired Mach numbers. High-fidelity data from adiabatic-wall simulations may be the best source of the information needed to anchor this extension into the new regime. Then, comparing those data to the isothermal-wall data presented here would allow for a more explicit investigation of the impacts of wall cooling and its proximate effects (e.g., changes in pressure or total temperature fluctuations in the BL profile). Further testing of the other components of the model derivation, like $\Lambda_\rho(y)$ is also warranted.

Acknowledgements

The authors gratefully acknowledge the funding support of SNL's Laboratory Directed Research and Development (LDRD) program. They would also like to recognize the contributions of Neal Bitter of the Applied Physics Laboratory at John Hopkins University and formerly of Sandia National Laboratories. He was instrumental in the setup and running of the cone DNSs.

References

[1] Jumper, E. J., and Fitzgerald, E. J., "Recent advances in aero-optics," *Prog. Aerosp. Sci.*, Vol. 37, 2001, pp. 299–339. https://doi.org/10.1016/S0376-0421(01)00008-2.

[2] Peck, E. R., and Khanna, B. N., "Dispersion of Nitrogen," *J. Optic. Soc. Amer.*, Vol. 56, No. 8, 1966. https://doi.org/10.1364/JOSA.56.001059.

[3] Clergent, Y., Durou, C., and Laurens, M., "Refractive Index Variations for Argon, Nitrogen, and Carbon Dioxide at λ = 632.8 nm (He-Ne Laser Light) in the Range 288.15 K ≤ T ≤ 323.15 K, 0 < p < 110 kPa," *J. Chem. Eng. Data*, Vol. 44, 1999, pp. 197–199. https://doi.org/10.1021/je980133o.

[4] Wang, K., and Wang, M., "Aero-optics of subsonic turbulent boundary layers," *J. Fluid Mech.*, Vol. 696, 2012, pp. 122–151. https://doi.org/10.1017/jfm.2012.11.

[5] Jumper, E. J., and Gordeyev, S., "Physics and Measurement of Aero-Optical Effects: Past and Present," *Ann. Rev. Fluid Mech.*, Vol. 49, 2017, pp. 419–441. https://doi.org/10.1146/annurev-fluid-010816-060315.

[6] Sutton, G. W., "Effect of Turbulent Fluctuations in an Optically Active Fluid Medium," *AIAA Journal*, Vol. 7, No. 9, 1969, pp. 1737–1743. https://doi.org/10.2514/3.5384.

[7] Gordeyev, S., Jumper, E. J., and Hayden, T. E., "Aero-Optical Effects on Supersonic Boundary Layers," *AIAA Journal*, Vol. 50, 2012, pp. 682–690. https://doi.org/10.2514/1.J051266.

[8] Gordeyev, S., Smith, A., Cress, J. A., and Jumper, E. J., "Experimental studies of aero-optical properties of subsonic turbulent boundary layers," *J. Fluid Mech.*, Vol. 740, 2014, pp. 214–253. https://doi.org/10.1017/jfm.2013.658.

[9] Wyckham, C. M., and Smits, A. J., "Aero-Optic Distortion in Transonic and Hypersonic Turbulent Boundary Layers," *AIAA Journal*, Vol. 47, 2009, pp. 2158–2168. https://doi.org/10.2514/1.41453.

[10] Hugo, R. J., and Jumper, E. J., "Applicability of the aero-optic linking equation to a highly coherent, transitional shear layer," *Applied Optics*, Vol. 39, No. 24, 2000, pp. 4392–4401. https://doi.org/10.1364/AO.39.004392.

[11] Gordeyev, S., Cress, J. A., Smith, A., and Jumper, E. J., "Aero-optical measurements in a subsonic, turbulent boundary layer with non-adiabatic walls," *Phys. of Fluids*, Vol. 27, 2015. https://doi.org/10.1063/1.4919331, 045110.

[12] Miller, N. E., Guildenbecher, D. R., and Lynch, K. P., "Aero-Optical Distortions of Turbulent Boundary Layers: DNS up to Mach 8," *AIAA Paper 2021-2832*, 2021. https://doi.org/10.2514/6.2021-2832.

[13] Butler, L. N., Gordeyev, S., Lynch, K. P., and Guildenbecher, D., "Development of a Spatially Filtered Wavefront Sensor as an Aero-Optical Measurement Technique," *AIAA Paper 2021-3123*, 2021. https://doi.org/10.2514/6.2021-3123.

[14] Castillo, P., Gross, A., Miller, N. E., Guildenbecher, D. R., and Lynch, K. P., "Wall-Modeled Large-Eddy Simulations of Mach 8 Turbulent Boundary Layer and Computation of Aero-Optical Distortions," *AIAA Paper 2022-*, 2022. submitted.

[15] Lynch, K., Spillers, R., Miller, N. E., Guildenbecher, D., and Gordeyev, S., "Aero-Optical Measurements of a Mach 8 Boundary Layer," *AIAA Paper 2021-2831*, 2021. https://doi.org/10.2514/6.2021-2831.

[16] Gordeyev, S., Rennie, R. M., Cain, A. B., and Hayden, T. E., "Aero-Optical Measurements of High-Mach Supersonic Boundary Layers," *AIAA Paper 2015-3246*, 2015. https://doi.org/10.2514/6.2015-3246.

[17] Gordeyev, S., and Juliano, T. J., "Optical Characterization of Nozzle-Wall Mach-6 Boundary Layers," *AIAA Paper 2016-1586*, 2016. https://doi.org/10.2514/6.2016-1586.

[18] Zhang, C., Duan, L., and Choudhari, M. M., "Direct Numerical Simulation Database for Supersonic and Hypersonic Turbulent Boundary Layers," *AIAA Journal*, Vol. 56, No. 11, 2018, pp. 4297–4311. https://doi.org/10.2514/1.J057296.

[19] Smith, J. A., DeChant, L. J., Casper, K. M., Mesh, M., and Field, R. V., "Comparison of a Turbulent Boundary Layer Pressure Fluctuation Model to Hypersonic Cone Measurements," *AIAA Paper 2016-4047*, 2016. https://doi.org/10.2514/6.2016-4047.

[20] Huang, J., Duan, L., Casper, K. M., Wagnild, R. M., and Bitter, N. P., "Direct Numerical Simulation of Turbulent Pressure Fluctuations over a Cone at Mach 8," *AIAA Paper 2020-1065*, 2020. https://doi.org/10.2514/6.2020-1065.

[21] Howard, M. A., Bradley, A. M., Bova, S. W., Overfelt, J. R., Wagnild, R. M., Dinzl, D. J., Hoemmen, M. F., and Klinvex, A. M., "Towards a Performance Portable Compressible CFD Code," *AIAA Paper 2017-4407*, 2017. https://doi.org/10.2514/6.2017-4407.

[22] Casper, M., K, Beresh, S. J., Henfling, J. F., Spillers, R. W., Pruett, B. O. M., and Schneider, S. P., "Hypersonic Wind-Tunnel Measurements of Boundary-Layer Transition on a Slender Cone," *AIAA Journal*, Vol. 54, No. 4, 2016, pp. 1250–1263. https://doi.org/10.2514/1.J054033.

[23] Marineau, E. C., Moraru, C. G., and Daniel, D. T., "Sharp Cone Boundary-Layer Transition and Stability at Mach 14," *AIAA paper 2017-0766*, 2017. https://doi.org/10.2514/6.2017-0766.

[24] Smits, A. J., and Dussauge, J.-P., *Turbulent Shear Layers in Supersonic Flows*, Springer Science+Business Media Inc., New York, 2006.

[25] Spina, E. F., Smits, A. J., and Robinson, S. K., "The physics of supersonic turbulent boundary layers," *Ann. Rev. Fluid Mech.*, Vol. 26, 1994, pp. 287–319. https://doi.org/10.1146/annurev.fl.26.010194.001443.

[26] Rumsey, C. L., "Compressibility Considerations for $k-\omega$ Turbulence Models in Hypersonic Boundary-Layer Applications," *J. Spacecraft Rockets*, Vol. 47, No. 1, 2010. https://doi.org/10.2514/1.45350.

[27] Pirozzoli, S., and Grasso, F., "Direct Numerical Simulation and analysis of a spatially evolving supersonic turbulent boundary layer at M=2.25," *Phys. of Fluids*, Vol. 16, 2004, pp. 530–545. https://doi.org/10.1063/1.1637604.

[28] White, F. M., *Viscous Fluid Flow*, McGraw Hill, New York, 2006.

[29] Hopkins, E. J., and Inouye, M., "An evaluation of theories for predicting turbulent skin friction and heat transfer on flat plates at supersonic and hypersonic Mach numbers," *AIAA Journal*, Vol. 9, 1971, pp. 993–1003. https://doi.org/10.2514/3.6323.

[30] Duan, L., Beekman, I., and Martín, M. P., "Direct numerical simulation of hypersonic turbulent boundary layers. Part 2. Effect of wall temperature," *J. Fluid Mech.*, Vol. 655, 2010, pp. 419–445. https://doi.org/10.1017/S0022112010000959.

[31] Hadjadj, A., Ben-Nasr, O., Shadloo, M. S., and Chaudhuri, A., "Effect of wall temperature in supersonic turbulent boundary layers: A numerical study," *Int. J. Heat Mass Trans.*, Vol. 81, 2015, pp. 426–438. http://dx.doi.org/10.1016/j.ijheatmasstransfer.2014.10.025.

[32] Guarini, S. E., Moser, R. D., Shariff, K., and Wray, A., "Direct numerical simulation of a supersonic turbulent boundary layer at Mach 2.5," *J. Fluid Mech.*, Vol. 414, 2000, pp. 1–33. https://doi.org/10.1017/S0022112000008466.